



Feasibility of Rotor Fault Detection from a Fluid Dynamics Perspective

S. L. Robbins^{1†}, P. S. Heyns¹ and J. A. Heyns²

¹ *Centre for Asset Integrity Management, Department of Mechanical and Aeronautical Engineering, University of Pretoria, Pretoria, 0002, South Africa*

² *Aeronautic Systems, Council for Scientific and Industrial Research, Pretoria, 0001, South Africa*

†*Corresponding Author Email: slrobbins94@gmail.com*

(Received February 10, 2020; accepted May 25, 2020)

ABSTRACT

The majority of condition monitoring techniques employed today consider the acquisition and analysis of structural responses as a means of profiling machine condition and performing fault detection. Modern research and newer technologies are driving towards non-contact and non-invasive methods for better machine characterisation. Yet current literature lacks investigations into the monitoring and detection of anomalous conditions using fluid dynamic behaviour. If one considers unshrouded rotors which are exposed to a full field of fluid interaction such as helicopter rotors and wind turbines amongst others, such an approach could potentially be beneficial. In this work, time-dependent fluid dynamic data is numerically simulated around a helicopter tail rotor blade using URANS CFD with the Open FOAM software package. Pressures are probed at locations in the field of the rotor and compared to results attained in an experimental investigation where good correlation is seen between the results. A blade is modelled with a seeded fault in the form of a single blade out of plane by 4° . Comparisons are drawn between the blade in its 'healthy' and 'faulty' configurations. It is observed that the fault can be detected by deviations in the amplitudes of the pressure signals for a single revolution at the probed locations in the field. These deviations manifest as increases in the frequency spectrum at frequencies equivalent to the rotational rate (1 per revolution frequencies). The results described are assessed for their fidelity when the pressure is probed at different locations in the domain of the rotor. Deviations in the pressure profiles over the surface of the blades are also seen for the asymmetric rotor configuration, but may prove too sensitive for practical application.

Keywords: CFD; Condition monitoring; Fault detection; Helicopter; Rotor; Unshrouded.

1. INTRODUCTION

1.1 Background

Rotating machinery considered in this study consist of a single rotor, where the rotor is unshrouded, and thus a full field of flowing fluid is present as a result of the turning rotor. Rotor blades which represent the rotating machinery class described include helicopter and wind turbine blades, amongst others, which are often slender, implying that their structural behaviour is likely to have a dependence on their aerodynamic behaviour and vice versa. When considering the condition monitoring (CM) procedures performed on most rotating machinery, structural responses are the prime focus of techniques and algorithms currently used. Even though this coupling between the structural and aerodynamic phenomena exists for these rotors, measurement of fluid dynamic

behaviour for the purpose of fault detection is not well represented in research or recognised as a useful means of assessing the condition of rotating machinery.

Helicopters experience high levels of vibration and noise with the main and tail rotors being large contributors towards this. The CM required to maintain general helicopter use is a prime example of the need to develop and improve the field since routine maintenance is responsible for its large running costs and time out of use.

This study sets out to investigate whether a seeded rotor fault can be inferred from the flow field. Studies of this nature have the potential to further a branch of condition monitoring techniques. It is envisaged that successful detection of rotor anomalies from the flow field may aid in better distinction between mass and aerodynamic imbalances experienced by rotor

systems. Furthermore, the eventual goal is to better describe the adjustments made to helicopter rotor systems when performing rotor track and balance procedures reducing its associated time and cost.

1.2 Literature Review

1.2.1 Rotor Condition Monitoring

Measurement techniques utilised for the condition assessment of helicopter and wind turbine composite rotor systems includes X-ray, computed tomography, infrared thermography, displacement sensors, velocity sensors, acceleration sensors, strain sensors, ultrasound, acoustic emission, shearography, laser Doppler interferometry and photogrammetry. The data acquired by these measurement techniques can then be analysed to find imperfections and anomalies, or the data may be processed such that the rotor is described in terms of characteristic parameters. Loading capabilities, deflections, fatigue limits, material stiffnesses, resonant frequencies, mode shapes and frequency response functions (FRFs) are parameters which describe the characteristics of the blade and can be compared to expected values or to the historical blade data.

The measurement techniques and fault indicators described attempt to identify rotor abnormalities which comprise of delaminations, voids, inclusions, cracks, dry fibres, defective fibre alignment, fatigue cracking, matrix cracking, de-bonding, fibre breakage, structural deformations, dirt or ice on the blade, erosion, corrosion, ultraviolet irradiation, lightning strikes, moisture absorption or imbalances. These fault mechanisms may arise as a result of the manufacturing procedure, installation error, failure of other components, exposure to the environment, material imperfections, fatigue, deterioration or due to its in operational dynamic behaviour. The techniques mentioned are some of the more common methods. Specific details on their application and use are discussed by (Pawar and Ganguli 2007; Hameed *et al.* 2009; Amenabar *et al.* 2011; García Márquez *et al.* 2012; Yang and Sun 2013). A number of the described techniques are based on measuring the vibrational responses of the rotor system and/or its components.

Over and above the monitoring of structural indicators for condition assessment, Hameed *et al.* (2009) and García Márquez *et al.* (2012) describe performance monitoring of wind turbines as an indicator of the overall condition of the rotor system. Analysing the expected power output of the rotor for given wind conditions can indicate potential problems in the event of abnormal operation. Moreover, Pawar and Ganguli (2007) report usage monitoring of critical components. The component life cycle is determined as a result of documented history and time in service, along with any known damage it has endured. The use of photogrammetry and other optical methods to monitor the dynamics of rotating machinery is an area of active research. This presents a means of taking measurements in a non-contact and non-invasive manner. However, in principle, the monitoring method measures displacements which are assessed in vibrational CM

frameworks and is thus still a function of the structural response (Pawar and Ganguli 2007; Ozbek *et al.* 2010; Gwashavanhu *et al.* 2016; Lundstrom *et al.* 2016).

Forbes and Randall (2013) successfully estimate the natural frequencies of turbine blades from the casing pressure and vibration measurements which are realised through an analytical model as well as experimentally. Although this study is performed for gas turbines, they state that the primary source which dominates casing vibration in a gas turbine is the aero/structure interaction of the internal pressure and the turbine casing. This is of particular interest as they further stipulate that this dominant excitation occurs as a result of three constituents, which they describe in their paper as:

- Blade pressure profiles which derive from the aerodynamic interactions around an unshrouded rotating blade,
- Transmission of acoustic waves within the rotor casing, and
- Pressure oscillations near the casing wall resulting from intensified flow conditions.

The force dominating the excitation of the turbine casing is the result of pressure fluctuations described in the first bullet point above. There might be a fundamental difference between the interactions for a shrouded and unshrouded rotor that exist due to the presence of the casing, but it is Forbes and Randall's description of the dominant factors which make up the pressure responses that are of interest. More so, the fact that the pressure signal retains diagnostic information while they describe the relationship between the pressure signal and the natural frequency of the blades to be dominated by the existence of a single faulty blade.

1.2.2 Imbalance

The imbalances which arise on rotor systems when in operation and consequently under dynamic loading are seen to comprise of two parts, mass and/or aerodynamic imbalances. Imbalances linked to either of these constituents may be a consequence of an asymmetric setup configuration but are often accentuated by rotor defects and incipient damage. This implies that the monitoring of imbalance is an important issue since the correction of imbalance relieves the system of any effect it has on the sub-systems connected to the rotor, such as the loads it transmits to the hub, bearing and drivetrain systems while it could also be indicative of inherent faults in the blade.

A method is proposed by Kusnick *et al.* (2015) to identify and correct rotor imbalance in wind turbines. The focus of the method is placed in distinguishing whether the imbalance is caused by a mass or aerodynamic (blade pitch error) imbalance by using a combination of parameters which include performance monitoring, hub loads and blade tip accelerations. Monitoring of the loads and vibrations transmitted to the rotor hub system from the blades indicates blade damage. The hub is expected to experience loads at harmonics relating to the number

(m) of rotor blades per revolution (i.e. mN/rev) with damage or faults detected as increases in the one per revolution (and its harmonics) responses. This is true for both helicopter rotors and wind turbine systems as described by [Pawar and Ganguli \(2007\)](#) and [Hameed *et al.* \(2009\)](#), respectively.

Dealing with helicopter rotor imbalances is referred to as Rotor Track and Balance (RTB). Helicopters experience large amplitude vibrations induced by the rotors at the same frequency as their rotation. RTB on helicopter rotor blades is the procedure followed in order to correct the mass and aerodynamic imbalance on the blades, consequently resulting in a reduction of those major rotating frequency components of rotor vibration. Rotor track is the path the blade follows through its rotation with the aim of the procedure being to ensure that each blade tip passes through the same vertical location, thus rotating through the same plane where the rotor is then said to be in perfect track. It is well known in the field of RTB that achieving perfect blade tracking alone may not result in vibration reduction. It is however still performed first in the effort of reducing asymmetric loading of the hub. Other adjustments are then made to further reduce vibrations where possible. RTB is performed by the addition/subtraction of weights and by making adjustments to the pitch control rods and trim tabs to achieve a perfect track and to minimise vibration amplitudes. The adjustments are determined by the operator and/or an algorithm based on data measured by an accelerometer in the cockpit of the aircraft and the tracking of the blades by the electro-optical method ([Renzi 2004](#)). The procedure described needs to be iterated to aid in determining the corrections to be made. While the method is effective, [Bechhoefer *et al.* \(2014\)](#) believe that there is room for improvements in the execution of RTB since algorithms are underdeveloped due to limited availability of data sets.

[Pawar and Ganguli \(2007\)](#) believe that there is a fundamental difference between rotor CM and RTB since RTB sets out to minimise the vibrations caused by rotor imbalance while rotor CM attempts to assess the structural integrity of a blade and isolate the damage. However, since vibration monitoring is an integral element in the execution of RTB, it is not uncommon for the vibration data to be used in identifying potential rotor damage ([Stupar *et al.* 2012](#)). The increased vibration levels might signify imbalance to be rectified by RTB or may be indicative of damage with further investigation required to distinguish between them. Such monitoring does not give detailed information as it detects some form of global defect and can potentially identify the component responsible but it simply focusses on the mechanical impact the fault propagates without actually identifying the fault mechanism or its location. Although, one might acknowledge that if blade tracking cannot be corrected by the described RTB procedure, blade damage is likely present.

1.2.3 Fluid Dynamic Models

When one considers the research efforts that have been dedicated to rotor modelling, particularly

helicopter rotors, the complexity associated with the problem becomes clear. Furthermore, it indicates the lack of a definitive model which can accurately predict the expected phenomena which include the wakes, dynamic stall, compressibility and shock interactions, reversed flow, all flow regimes, unsteady flow, blade vortex interaction (BVI – the interaction of the vortices produced by each of the helicopter rotors) as well as a fair representation of the structural dynamics of an articulated blade from fluid-structure interactions (FSIs), rigid body motion and deformations. In fact, certain instances of the phenomena mentioned are specialist fields and have uncertainties and complexities of their own which prohibit their successful modelling. [Bramwell *et al.* \(2000\)](#) indicate that much of helicopter theory can be deduced when one regards the blade as rigid and understanding the underlying assumptions made to implement such simplifications. This is supported by [Conlisk \(1997\)](#) who also mentions that due to the complexities which present themselves when modelling rotors, investigations need to be well-targeted in scope so that significant simplifications can be made in order to focus on specific aspects of the flow.

In consideration of studies which are scoped to understand the aerodynamics related to rotors, [Pandey *et al.* \(2012\)](#) conducted a numerical simulation on a helicopter rotor blade. They performed a single computational fluid dynamic (CFD) simulation on an isolated helicopter rotor blade for a specified rotational speed and angle of attack said to represent hovering flight conditions. The only objective of their study was to analyse the flow around the rotor for these conditions where comments are made on the presence of the vortex sheet in the plane of the blade and the concentrated tip vortices.

A CFD analysis on a vertical axis wind turbine (VAWT) under fault conditions consisting of missing blades is considered for CM by [Park *et al.* \(2012\)](#). They monitor VAWT output performance, noting a significant degradation as blades are removed. [Oggiano *et al.* \(2016\)](#) use URANS CFD to model a horizontal axis wind turbine (HAWT) with a single blade off-pitched to emulate imbalance and for comparison with experiments. They discuss the effect of the off-pitched blade on the torque and axial force experienced by each blade as well as the rotor in total and also report a drastic decrease in output performance with the fault. Another study which uses performance output to monitor rotor condition was completed by [Allmark \(2016\)](#). This study considers a CFD analysis of tidal stream turbines with off-set pitch blades to simulate rotor imbalance faults to develop CM and fault diagnostic techniques.

As a consequence of fluid interactions, acoustic analysis and noise generation are studied, allowing one to delve deeper into the exploration of aerodynamic behaviours. [Strawn and Biswas \(1996\)](#) simulate aerodynamics and acoustics of a helicopter rotor blade. Their analysis is performed on a non-lifting (zero pitched) rotor to match experimental data. Good agreement is found for the in-plane acoustic pressures (impulsive noise) generated by the

blade between the experimental and simulated results. [Li *et al.* \(2016\)](#) study the effects on the performance and aeroacoustics of a shrouded axial fan when there is a blade with an abnormal angle (different pitch to the other blades). They observe the abnormal blade to cause a degradation in fan performance and a rise in aero-acoustic noise simulated with a 3D large eddy simulation (LES) model which illustrates the ability of fault detection from aero-acoustic noise.

1.3 Motivation and Scope of Research

Current literature clearly illustrates the dominance that structural response and analysis possesses over any form of fluid dynamic based rotor CM and diagnostics. It is also true that much of rotor modelling focusses on model accuracy (both structural and aerodynamic) and, in cases which do introduce fault mechanisms, mostly model structural responses. Fluid models which do consider rotor faults generally monitor power output performance characteristics for anomalous behaviour and are considered for a small host of faults.

The work of [Forbes and Randall \(2013\)](#) and [Li *et al.* \(2016\)](#) where pressure signals are used to estimate blade natural frequencies and aerodynamic noise is used to detect an off-pitched fan blade, support arguments that the fluid carries diagnostic information about the rotor when in operation. These studies considered a shrouded rotor. To the authors' knowledge, there are no studies which consider the fluid dynamic behaviour of an unshrouded faulty rotor for CM purposes.

The focus of this study is not on the development of a detection algorithm, nor is it on the signal processing. Instead, this study assesses the feasibility of detecting a rotor fault from flow field data using a fluid dynamics model. This is in an effort of establishing a foundation of what one could infer from the flow field about machine condition. This numerical investigation is supplemented with an experimental investigation in order to validate the results, this also serves as an example of practical application. One of the potential benefits of fluid dynamic based CM that this study alludes to is the distinction of aerodynamically induced rotor imbalance from mass imbalances since conventional measurement techniques couple the two to measure the net influence of imbalance.

The analysis is performed on a helicopter tail rotor blade which serves as a representative for unshrouded rotors. Analysing a tail rotor as opposed to the main rotor is advantageous as it allows a considerable reduction in the complexity of the problem; its structural and fluid dynamic behaviours are less pronounced than for the main rotor yet they are still present enough to provide a meaningful analysis. The rotor blade is assessed at a constant rotational speed (conducive of normal operation), a zero pitch and without the effects of any external interactions. A RTB fault in the form of mistracking is imposed as a rigid out-of-plane displacement of one of the blades in the numerical investigation. The flow field around the rotor blade is modelled using a transient URANS analysis for instances of a healthy

and faulty rotor which are compared to assess the flow fields for fault detection features. This implies that the rotor is modelled as rigid to avoid the complexity of dealing with the flexibility of the composite rotor under aero-elastic effects.

2. EXPERIMENTAL METHODOLOGY

Experiments were conducted in order to collect data which shall be used for comparison and thus validation of the simulations of the helicopter rotor blade. It also allows the study to emulate a scenario of measurement techniques which provides a better understanding of what is practical. This chapter describes the rotor blade that was used and the experimental setup used to capture pressure data.

2.1 Tail Rotor Blade

The tail rotor selected comes from an AS350 helicopter (both the B2 and B3 variants) with part number 355A12-0040-08. Table 1 gives some of the specifications of the tail rotor blade which were taken from the systems manual used by helicopter technicians.

Table 1 Specifications of helicopter tail rotor blade

Composition of tail rotor	Composite materials
Actual chord	185 mm
Locally in the tab area	205 mm
Rotor diameter	1860 mm
Symmetrical airfoil profile	NACA 0012
Theoretical twist	0°
Wedging of strap in torsion area	10°
Pitch axis rotation	37 mm from leading-edge
Number of blades per rotor	2
Rotational speed (max. regulated)	2147,3 RPM
Rotational speed in autorotation	2472.8 RPM
Power	1140 kW

Figure 1 summarises the overall dimensions of the rotor blade in a simplified sketch. The NACA 0012 airfoil profile runs from the inner diameter of 540 mm to the tip of the blade.

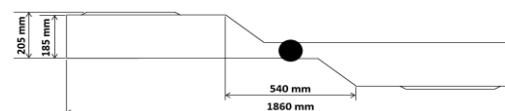


Fig. 1. Overall dimensions of tail rotor blade.

2.2 Experimental Setup

The experimental investigations of [Xu and Amano \(2002\)](#) and [Xu *et al.* \(2002\)](#) were used as a basis around which to formulate the experimental work

considered in this investigation. In their investigations, unsteady pressure field measurements of an axial flow fan were taken on the blade and at the inlet and outlet of the fan using a rake of transducers, respectively. Taking measurements on the blade requires more sophisticated equipment and setup time increasing the complexity of the procedure which is undesirable for CM purposes. Flow field measurements were taken in the field of the rotor at specific locations which is simpler and more practical. This represents measurements taken at stationary points in the field or at fixed locations on the helicopter.

The helicopter tail rotor blade was attached to a shaft which had a sleeve to control both blade pitches uniformly. The shaft was positioned by two bearing houses. A 7.5 kW electric motor powered the shaft through a belt and pulley system, as shown in Fig. 2. Zebra strips were pasted on the shaft that were read by a laser tachometer to determine its speed. The power supplied to the electric motor could be controlled which adjusted the speed of the rotor. The pitch of the blade was measured by placing a tilt sensor (inclinometer) at 30% of the chord length of the blade as it is the position which has the maximum height along the chord and should be parallel to the chord line of the aerofoil.

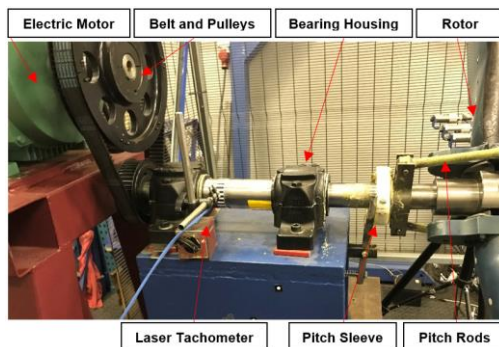


Fig. 2. Rotor shaft setup.

Three WIKA P-30 pressure transducers were attached to a frame to form a radial rake of measurements. The transducers were positioned at radial distances of 67%, 80% and 100% of the rotor radius, i.e. 620mm, 744mm and 930mm (at the tip) from the centre of the rotor. The stand for the rake was then positioned such that the pressure probes were parallel to the blade and perpendicularly placed at a distance X, shown in Fig. 3. Marker X in Fig. 3 was measured from the trailing edge of the blade (the chord line when using zero pitch) to the opening of the WIKA sensor for pressure measurement. Values of X for which data was captured were 20mm and 100mm, producing a total of 6 time-dependent pressure measurements. The setup of pressure transducers are shown in Fig. 3 and Fig. 4.

Finally, Fig. 5 depicts the overall setup for the experiments. The power supply used for the transducers and the data acquisition unit which the equipment was wired to for data recording can be seen. The data acquisition unit was set to record at

19.2 kHz, power was supplied to the motor and ramped until it reached its maximum capacity where recording continued for a few seconds to acquire steady conditions.

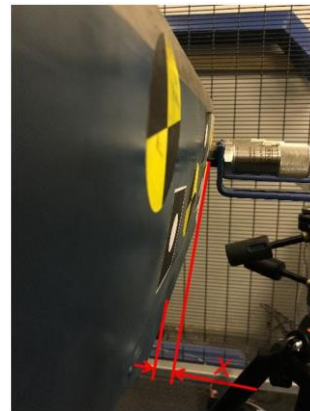


Fig. 3. Perpendicular distance X.



Fig. 4. Transducer positioning.

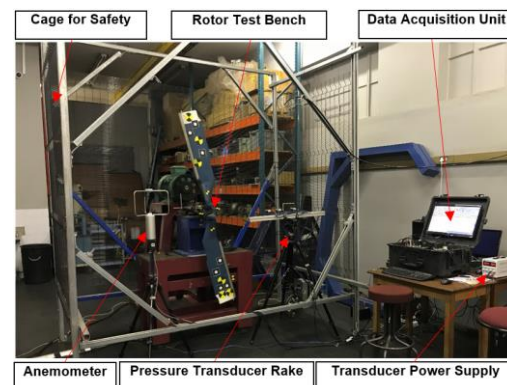


Fig. 5. Complete experimental setup.

A cage that was constructed around the rotor test bench can be seen in a few of the figures. This was for safety purposes. An anemometer is also seen in the experimental setup which was connected to the data acquisition unit and for which data was recorded during the experiments. The results produced by the anemometer were discarded as it collected data at a maximum output frequency of 32 Hz which was insufficient in capturing any useful transients when the helicopter rotor was ramped up to full speed.

The maximum rotational speed achieved by the rotor test bench was with a zero-pitched rotor due to the power restrictions of the electrical motor. Increasing the pitch of the blade increases the drag experienced by each blade and thus the torque required. Using an electrical motor at its maximum power results in the rotational speed being reduced with the increased torque. The experiments were performed with a zero-pitch blade so that the maximum rotational speed could be used for this investigation. For the two tests conducted a maximum average of 1830 RPM was achieved. A zero-pitched rotor does not emulate the operational conditions of a helicopter rotor and the rotational speed acquired in the experimental investigation is lower than that specified for the particular rotor in Table 1. However, these conditions are good for the purposes of this study as one can still draw useful conclusions from the described investigation. Also, consider that Singh *et al.* (2008) simulate a tail rotor speed of 1564 RPM in their research while Strawn and Biswas (1996) use a zero-pitched rotor in their study of helicopter rotor aerodynamics and acoustics.

3. NUMERICAL METHODOLOGY

The cases which were constructed in order to simulate the flow around the rotor blades required pre-processing steps such as the definition of the rotor geometry, its domain and the generation of a mesh. A description is given on these steps as well as parameters prescribed in the case files to run the simulations in OpenFOAM. Finally, the solving strategy used for this investigation is defined.

Note, two full rotor simulations were executed in this investigation. The simulation relating to the perfectly symmetric rotor will be referred to as the healthy simulation whereas the simulation relating to the rotor with a mistracked blade shall be referred to as the faulty simulation.

3.1 Rotor Geometry and Domain

The rotor geometry was defined by following the specifications provided for the tail rotor and using the NACA 0012 airfoil with a 185 mm chord length. Figure 6 portrays the model generated for the healthy rotor. The rotor geometry was simplified from the true geometry to exclude unnecessary details, which include the modelling of the hub region as well as the removal of the trim tab. It is understood that the trim tab affects the aerodynamics of the rotor but it is not within the scope of this investigation to study its effects directly. This study considers the overall effect of blade mistracking which may be affected by trim tab arrangements and can be considered independently in further investigations. The geometries are modelled such that they rotate about the positive y-axis and extend radially into the z-axis at time zero.

The faulty (or mistracked) rotor was modelled identically to the healthy rotor apart from offsetting one of the blades. Figure 7 shows both the healthy and faulty rotor blades where one can see the geometric offset that has been imposed to one of the blades in the faulty configuration. At time zero, the

blade situated in the negative z-direction was offset by 4° into the negative y-direction.



Fig. 6. Healthy blade model.



Fig. 7. Healthy and faulty blade model showing offset blade.

After modelling the rotor geometry, the domain was defined to set the extent of the boundaries wherein the fluid flow will be solved. Figure 8 shows the domain modelled around the rotor blade. The rotor was situated at the centre of a 3.86 m diameter and 1 m high cylinder. The boundary locations were constrained to these dimensions to restrict the computational expense of the simulations. Using the domain extents described in Fig. 8 does have the advantage that it resembles the experimental setup of the rotor in the laboratory as the radial boundaries emulate the restriction of the walls. The top and bottom circles as well as the cylindrical wall which connects the two surfaces make up the boundary wall while the rotor surfaces make up the rotor wall for the prescription of the boundary conditions.

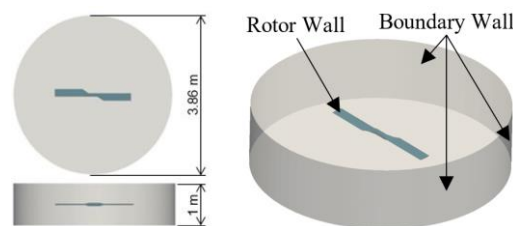


Fig. 8. Model domain boundary locations.

3.2 Meshing

Investigative studies were performed on 2D cross-sections of the rotor blade and validated against data from literature at speeds of Mach 0.3 and Mach 0.5. These speeds represent linear velocities at radial locations of 0.54 m and 0.90 m, respectively, thus representing a considerable portion of the rotor blade. The use of wall functions to model the viscous sublayer and buffer layer of the boundary layer

Table 2 Model boundary conditions

	$\text{nut} - \nu_t$	$\text{nuTilda} - \tilde{\nu}$	p	U
Internal Field (IC)	0.75v (1.10E-5)	4v (5.84E-5)	0	0
Rotor Wall	Wall function (0)	Fixed value (0)	Zero gradient	Moving Wall Velocity
Boundary Wall	Freestream (1.10E-5)	Freestream (5.84E-5)	Zero gradient	Zero gradient

provides an economical alternative to resolving them directly. This implies that the first cell off the wall is required to possess a y^+ value of between 30 and 500 which provides enough resolution to capture the log-law layer while the wall function models the effects of the lower layers. Mesh independent solutions were acquired whose y^+ values along the surface of the airfoil abided by the described law of the wall for near-wall treatment flows at both speeds. The results produced by these studies were dependable based on their correlation with the validation sources, one of which was followed closely and is presented by (Rumsey 2016). The studies produced cell heights between 0.65 mm – 0.9 mm for the first mesh cell from the surface of the airfoils. This value was used to define the mesh of the rotor setups since it would be computationally uneconomical to do a mesh independence study on the full rotor case.

Figure 9 provides a number of screenshots of the mesh that was generated for the healthy rotor where the meshing strategy can be seen. The mesh was dominantly structured and cell heights were linearly stretched such that areas anticipated to have high gradients and require good resolution were biased to have smaller cell heights. The mesh stretched from these regions with the prescribed cell height off the rotor wall to the boundaries reducing the number of cells generated in the mesh and saving computational expense. This ensured that the tip of the blade, its wake and the flow field in the direct vicinity of the rotor blade was resolved well. A mesh of approximately 7.2 million cells was produced.

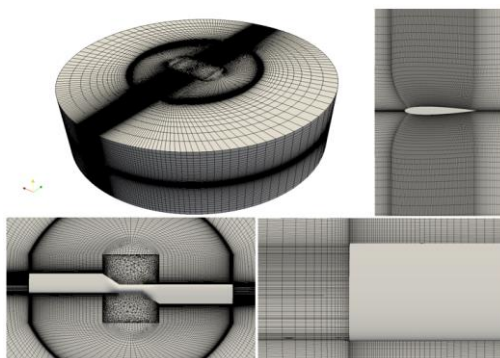


Fig. 9. Mesh generated for healthy rotor.

Figure 9 reveals that in most regions, the mesh is of good quality with the exception of the centre region

where the hub is located. This region was meshed last in the meshing order and used an unstructured mesh to patch together all of the other structured regions. A general rule of thumb when generating meshes for CFD is that the transition from one cell to the next should not experience a length change greater than 30%. This is obeyed throughout the domain except for the transitioning of the mesh from the other regions to the hub region. This was the only known issue of the generated mesh which could not be rectified without affecting the remainder of the approach and severely impacting the mesh quality metrics. Exceptionally poor quality metrics resulting from adjustments to the above meshing approach prevented the simulations from starting as they were too unstable. Despite this issue, the mesh depicted in Fig. 9 was used for the simulations. The healthy and faulty rotors were meshed according to the same strategy producing similar meshes where some deviations might be present in the centre region due to the unstructured mesh used.

3.3 Case Parameters and Solving Strategy

The investigative studies alluded to in the previous section were also used to select the turbulence model and assess the necessity of using a compressible solver. It was found that at a speed of Mach 0.5 (representing a radius of 0.90 m) a maximum error of 12.75% was found at the peak pressure drop on the surface of the airfoil when using an incompressible model. The scope of this study was not targeted at accurately modelling the performance of the rotor blade which allowed the decision to neglect compressible modelling. The analysis performed also provided evidence that there was no significant difference between the Spalart Allmaras and k-Omega SST turbulence models for the zero-pitched rotor and that turbulence could be assumed over most of the rotor length. Selection of an incompressible model and the Spalart Allmaras turbulence model allowed for the construction of an economical model with a minor trade-off on accuracy.

The pimpleDyMFoam solver was used in OpenFOAM-v1612+ which allowed the mesh to rotate dynamically, producing incompressible transient results. A rotational speed of 191.64 rad/s (1830 RPM), the Spalart Allmaras turbulence model and properties for air at standard conditions were prescribed in the respective case files. Table 2 summarises the boundary conditions prescribed for

each of the field variables. The values for the turbulent quantities were based on their relation to the kinematic viscosity of air as described in the derivation of the Spalart Allmaras turbulence model. The rotor wall was prescribed the nutUSpalding wall function for the turbulent viscosity and a relative velocity to the dynamic mesh of 0.

The Centre for High-Performance Computing (CHPC) based in Cape Town, South Africa provided the computational resources on their Lengau Dell Linux cluster to run the simulations. The cases were decomposed into 120 subdomains and run on a high performance computing cluster in parallel. Initially, first-order discretisation schemes were used allowing the dissipation of transients and to increase numerical stability so that divergence was avoided. Once the simulations had dissipated any erratic transients, second-order discretisation schemes were used for the remainder of the solution. The feature in OpenFOAM which allows the specification of running the simulation with a maximum courant-friedrichs-lewy (CFL) number as opposed to a fixed time-step was used. As an extra means of ensuring stability, the maximum courant number prescribed for the simulations was ramped as the simulation commenced starting with a maximum CFL as low as 2 and allowing the solution to converge for a value of 10.

With the computational resources used for the simulations and the solving strategy implemented, the simulations were still demanding requiring numerous runs. A simulated time of approximately 0.024 seconds took 48 hours to compute when using 120 cores on the cluster. The solving strategy could not be adjusted too much to speed up the runs since increasing the maximum courant number resulted in the simulation diverging.

The locations at which pressure and velocity were probed in the field of the rotor are shown in Fig. 10. Probes 0 to 5 correspond to the experimental locations at which data was captured in the field of the blade. Pressures and velocities at these locations were monitored for convergence along with the rotor moments, forces and the residuals of the field variables. These parameters were monitored for steady behaviour which meant that for most of the parameters steady periodic oscillatory behaviour signified convergence as it is a transient analysis. Once convergence was identified, the solution was allowed to develop for a further 4 full revolutions of the rotor to produce converged data for analysis.

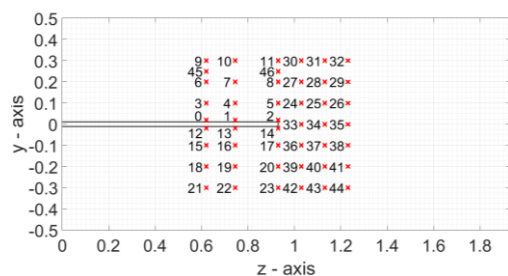


Fig. 10. Location of simulation probes in domain.

4. RESULTS AND DISCUSSION

This section presents pressure signal comparisons in both the time-domain and frequency-domain. The signals are filtered for time-frames of constant rotational speed (experiments) or for converged results (numerical). The signals are converted to Pascals from their standard measurement units and their means are subtracted (to remove any DC offset). Instabilities in the numerical pressure results caused by simulation restarts are dampened. The signals are then time synchronously averaged to represent the pressure at the respective locations for a full revolution of the rotor. The non-averaged signal was transformed into the frequency domain using a fast-fourier transform (FFT).

4.1 Validation of Results

The numerical results produced by the simulations for the healthy rotor blade are compared to the experimental results for validation and to assess the integrity of the simulations in representing the physical phenomena. Validating the simulations also provides a basis on which model-based CM and fault detection can be used to represent actual scenarios. Figure 11 compares the time-synchronously averaged signals over a single revolution for the experiments and the healthy simulation at probes 0 to 5. The maximum and minimum values recorded during the experiments are also plotted as dotted lines.

The simulations predict the crests and the troughs of the pressure profiles at each location well. Probes 3 to 5 appear to match the experiments better than probes 0 to 2. However, experimental probes 0 to 2 feature a larger variance in its peak values which is evidenced by the difference between the maximums, minimums and averaged signals at each probe as well as the presence of the fluctuations inherent in the averaged signals, specifically after the blade had passed which may indicate the presence of trailing vortices and other transients disturbing the flow near the blade and in its wake. These fluctuations are not well represented by the simulated probes which are most likely due to the limitation in using URANS modelling as it would not be able to model disturbances at these frequencies. Even though these discrepancies are present, the numerical results at these closer locations are still within reason of modelling the pressures at these locations as they represent the experimental signals appropriately and are within their maximum and minimum bounds. A visible distinction is also seen at probes 2 and 5 since these probes are situated at the tip of the rotor. Again, disturbances affect the profile of the experimental pressures but the simulated signal of probes 2 and 5 resolve the drop in the pressure peaks at these locations in comparison to the peaks at probes 1 and 4. The numerical results at probes 3 and 4 resemble the experimental results impeccably. It is compelling to see that the numerical results produce troughs which are near identical for each blade passing. A static analysis of the experimental test bench, in which each of the blade tracks was measured with respect to a fixed location, found that the tips were 15

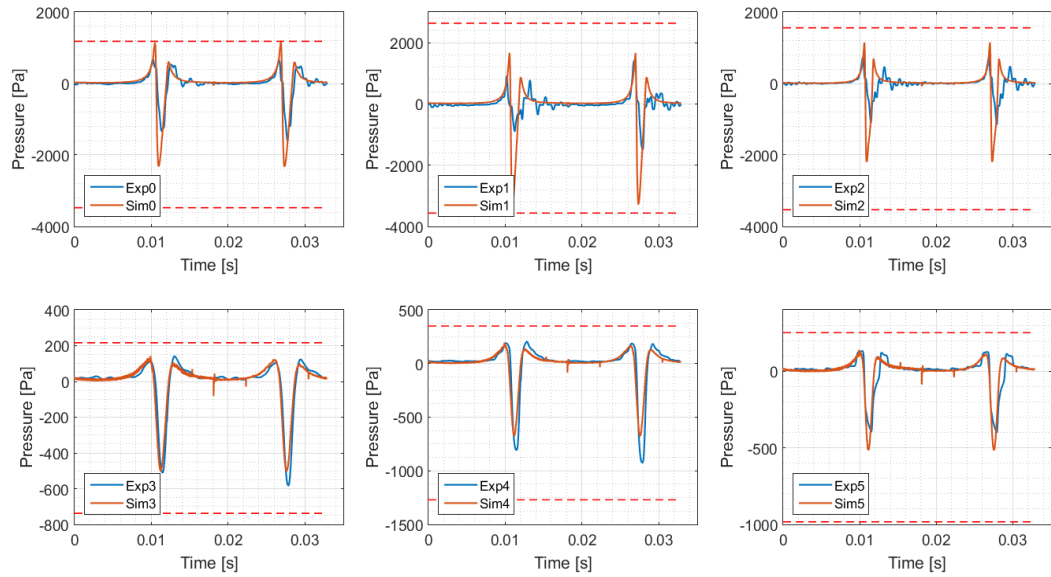


Fig. 11. Comparison of experimental and numerical pressure profiles.

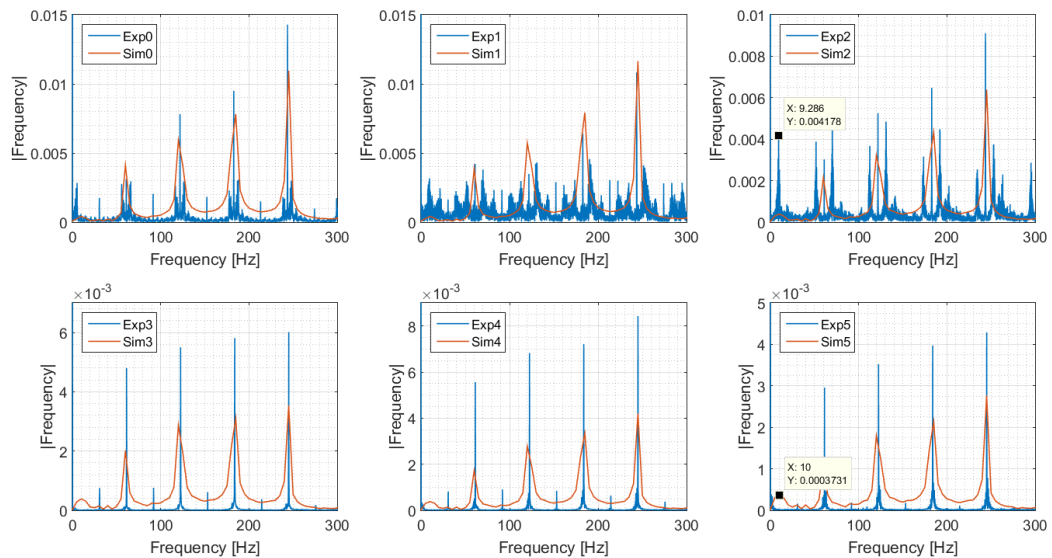


Fig. 12. Comparison of experimental and numerical frequency content.

mm out of track (i.e. a single blade was approximately 0.95° out of plane with respect to the hub). Even though the level of mistracking was not substantial, it evidences that the experimental investigation was not conducted with a blade which tracked perfectly. Importantly, this is shown in the different peak levels of the results which the investigation sets out to prove. It is also noteworthy that this degree of mistracking features in these results considering they were time-synchronously averaged. Small spikes observed in some of the numerical results are again attributed to the instabilities caused by simulation restarts which could not be completely damped.

Figure 12 compares the frequencies for the experiments and the healthy simulations at probes 0 to 5. Be aware that the numerical frequency

amplitudes had to be scaled for the comparison so it is only the peak frequency components that are of interest. The comparisons of the frequencies show that all of the numerical probes predict the blade pass frequency (≈ 61 Hz) and all of its harmonics well correlating with the experiments. Unlike the experiments, the numerical probes do not observe frequencies at the rotational frequency (≈ 30.5 Hz) which describes the experimental blade mismatch while the healthy simulation had near-identical profiles for each blade passing thus identifying the blade pass frequency only.

Note that the numerical results predict a low-frequency component at approximately 10 Hz but do not display any sidebands like the experimental work. [Xu *et al.* \(2002\)](#) describe this low-frequency component to be a result of aerodynamic delay which

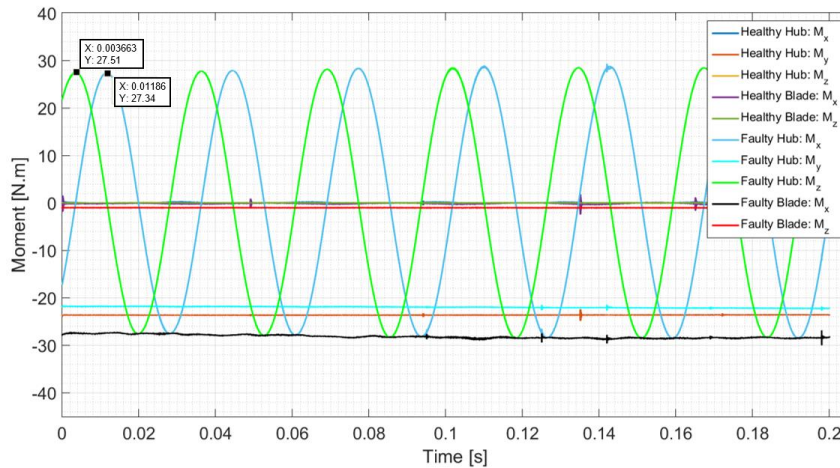


Fig. 13. Comparison of healthy and faulty rotor moments for hub and blade reference frames.

one can see is modelled well. The simulations are incapable of modelling the sidebands aside the blade-pass and rotational frequencies in the experiments. These may be indicative of the blades flapping or vortex shedding which the current simulation is incapable of modelling due to the rigid rotor assumption and the use of RANS turbulence modelling. It is likely that the modulation is due to one of these components, as opposed to other factors such as pressure rebounds from the laboratory walls or the presence of the safety cage, because of the dependence of the modulation on the positioning of the rake. Transducers 0, 1 and 2 clearly show sidebands unlike transducers 3, 4 and 5 implying that one might expect to see the effects from the laboratory or safety cage at the same amplitude in the results at both rake locations but they are not and are diminished in the transducers placed further away.

It can be concluded from this section that the numerical results correlate well with the experiments and thus model physical phenomena well. Frequencies caused by occurrences such as blade flapping or fluctuations from other fluid dynamic behaviour cannot be modelled but are not of interest. The results indicate that pressure troughs and frequencies in the order of the rotor rotation and blade passing are modelled well and are of more interest in light of fault detection.

4.2 Fault Detection

Comparison of the results delivered by the healthy and faulty simulations can be conducted to assess the flow field information to see in what ways the blade asymmetry can be inferred and thus detected. The following sections consider fault detection strategies from the results produced by the simulations.

4.2.1 Force and Moment Analysis

The dynamic mesh model used in the simulations rotates the entire mesh during the simulations where quantities are prescribed according to a stationary coordinate system. Results for the stationary frame (or global coordinates) shall be referred to as the hub results since forces and moments of this type would

be measured at stationary locations situated at the hub of the rotor system. Alternatively, results which make reference to the blade refer to a local coordinate system which ‘follows’ the blade as it rotates. This corresponds to measurements taken on the blade throughout its rotation. The blade results were determined by performing a coordinate transformation of the hub results for the x and z components as the blade rotates.

Figure 13 gives the results acquired for the moments for both the healthy and faulty simulations at the hub and blade reference frames. Considering the hub loads first, the healthy rotor illustrates minute fluctuations around 0 for the x and z-components while reporting a mean value of -24 Nm for its y-component. These values reflect the healthy simulation well since values of 0 for the x and z-components reflect the blades symmetry while the larger negative value for the y-component reflects the torque required to rotate the blade. The x and z-components transformed to the local blade reference frame reflect similar findings with mean values of 0 reported.

Comparing the results for the faulty blade at the hub, considerable differences are observed. The x and z hub components fluctuate between high moment values. These two components are phase-shifted by a 90° rotation of the blade which is clearly based on the time instances at which the measurements align with the hub coordinate system. It is also intriguing to note the minor decrease in the y-component for the faulty rotor at the hub. The transformed x and z-components for the faulty rotor show that in a reference frame which follows the blade, there is a small negative z moment and a large negative x moment. Considering the imposed fault, these conclusions are logical as the lift of the two mistracked blades is enforced in two different planes causing a twist about the x-axis.

Transforming each of these signals into the frequency domain reveals that there are no other noteworthy frequency components apart from large amplitude increases in the x and z hub components at the frequency of the rotational speed. This is apparent by simply observing the trends shown in Fig. 13.

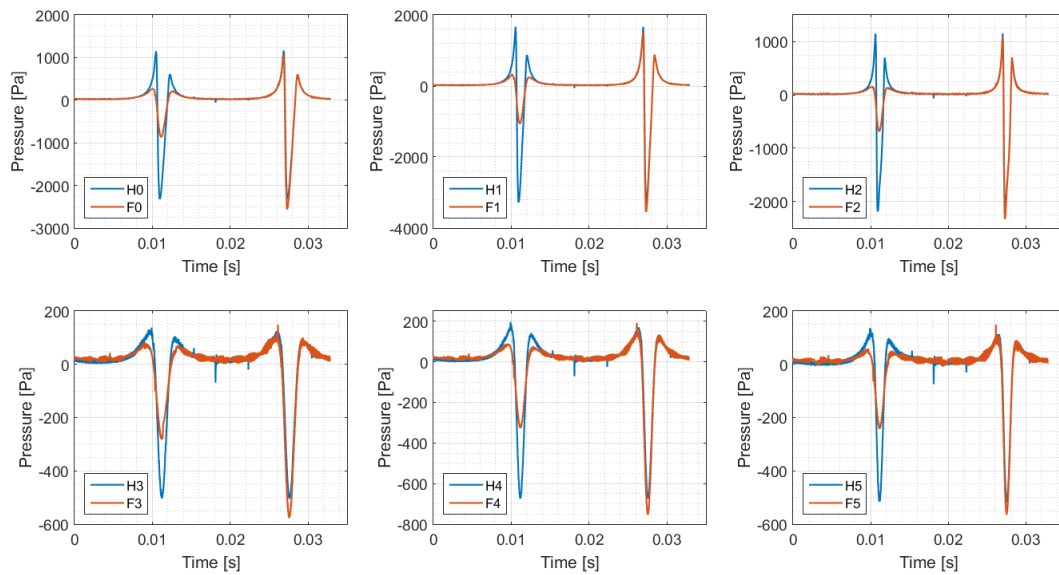


Fig. 14. Comparison of healthy and faulty pressure profiles.

Analysing the results for the forces experienced at the hub and blade reference frames presented similar findings.

The literature review identified numerical investigations which have performed CFD analyses under faulty rotor conditions. Most of these studies used the force and moment (or torque for performance analysis) information for fault finding and nothing else. The results described above for the helicopter rotor simulations serve as further proof of these analyses since it confirms that the presence of a fault increases the 1/rev amplitudes of force and moments encountered which the studies in literature also found. However, acquiring these measurements practically for CM purposes is difficult and, where possible, does not eliminate the issue of identifying the specific fault since most rotor faults would manifest in this response. Measurements on the blade are undesirable due to their complexity and expense. It would also be difficult, if possible, to measure force and moments about the other axes at the hub of the rotor. Finally, increases in the 1/rev force and moment amplitudes would result in vibrations at this frequency which could be measured in the aircraft. This is already done in RTB procedures and although the vibration levels could signify a fault they do not aid in identifying and isolating the specific fault. It can be concluded that force and moment data does provide diagnostic information but is difficult to implement practically which serves as motivation for seeking alternative means of rotor fault detection, where fluid dynamic monitoring may have the potential to be a simplistic, cheap and viable option.

4.2.2 Pressure Probe Analysis

Figure 14 compares the time-synchronously averaged signals over a single revolution for the healthy and faulty simulations at probes 0 to 5.

To varying degrees, each of the probes in Fig. 14 show a reduction in the pressure trough when the

faulty blade passes. A reduction (as opposed to an increase) in the trough is expected since all of the probes pictured are situated in the positive y-axis while the blade was deflected into the negative y-axis. This phenomenon clearly demonstrates that a rotor which is out of track is expressed as non-symmetric troughs in the time-domain. This is substantiated by the experimental results of Section 4.1 whose pressures were non-symmetric having been recorded for a rotor which was out of track. One should also note the phenomenon of the slight amplitude increase for the blade that tracks perfectly on the faulty rotor in comparison to the stable symmetric troughs for the healthy rotor. This might be caused by the perfect blade rotating through flow that is more orderly than when it passes through the other blades wake, causing an adverse pressure gradient and disturbing the flow more.

Figure 15 compares the frequencies for the healthy and faulty simulations at probes 0 to 5. It is clear that the fault arises as increases in the amplitudes of the frequencies at the rotational frequency of the rotor (1/rev frequency). This is again supported by the results produced in Section 4.1 since frequencies at the rotational frequency were observed for the out of track rotor. Comparing the 1/rev frequency amplitudes exhibited at each probe location, probes 0 and 1 have similar amplitudes and are the highest amongst all the probes. Probes 3 and 4 also reproduce similar amplitudes but are smaller than probes 0 and 1 since they are located further away from the blade. Probes 2 and 5 see major reductions in their amplitudes in comparison to their rake counterparts and can again be attributed to the loss in pressure due to tip vortices. All probes for both rotor configurations display high-frequency amplitudes at the blade pass frequency and its harmonics. The pressure signals for the faulty blades appear to decrease the amplitudes of the harmonics at these frequencies slightly.

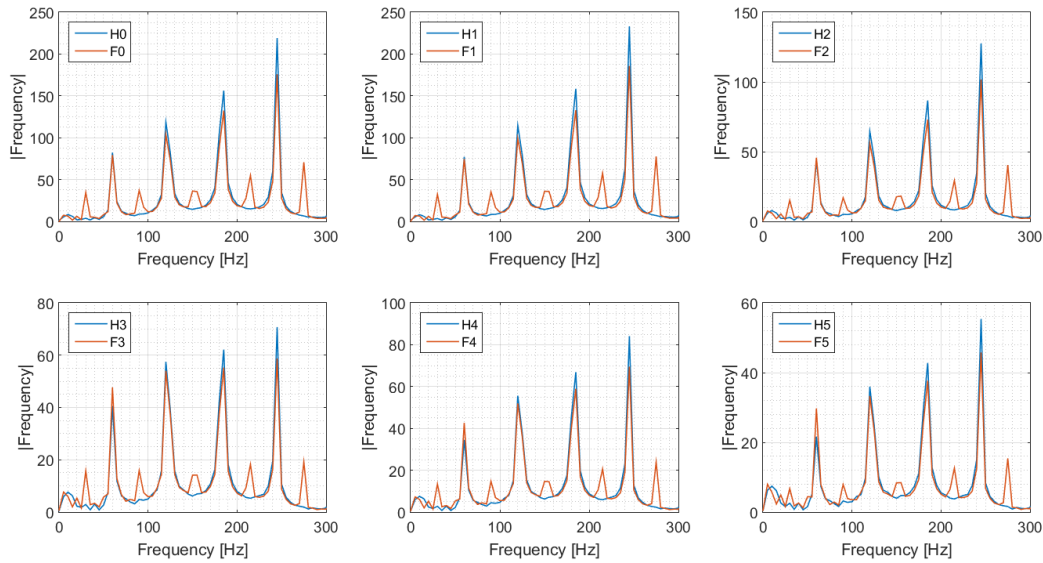


Fig. 15. Comparison of healthy and faulty frequency content.

The above discussion proposes fault detection features from simulated pressure data presented as a time-synchronously averaged signal and in the frequency domain. The use of a rigid rotor assumption and RANS turbulence modelling means that the simulations are not capable of representing phenomena such as blade flap and vortex shedding. This means the model fails to represent components of the pressure signal which are realistic contributors as seen in Section 4.1. One might argue that these components could deteriorate the fault detection capabilities of the features introduced above. However, even though the simulations are not able to replicate certain phenomena they demonstrate the response of the fault mechanism independent of the effects of blade flap and vortex shedding. This means that the fault is easily observed as the primary source of the features identified. It is also the case that the phenomena which are absent in the simulations presented themselves through other features such as the sidebands of the carrier frequencies which are not present in this analysis nor important to the fault detection strategy mentioned. Another consideration of how the results might be affected could be due to the neglected phenomena on the troughs of the pressure signals in a practical environment. One might say that the time-synchronous averaging is necessary since it separates the discrete and random components of the pressure signal, where the random components include the blade flap/vibrations and the vortices which cause the signal to fluctuate. This provides the averaged signal which can be analysed for its behaviour and to assess the presence of fault features. Confidence in the fault detection feature is drawn from the fact that the experiments were conducted under faulty conditions and was capable of detecting the rotor asymmetry despite the presence of these components.

The presence of the fault in Fig. 14 can be described by saying that as the faulty blade passes further away from the probe locations it produces smaller pressure

gradients and blunter peaks in the profile. The asymmetry of the troughs corresponds to how the fault features in Fig. 15. This description implies that, in theory, one might expect these features to depict the severity of the fault. Furthermore, these results prove that rotor asymmetry is presented as increases in the 1/rev frequencies but this would be the case for a number of aerodynamic based fault mechanisms. Comparison of the time domain pressure profiles for the different blades provides valuable information about the fault. In this instance, the faulty blade is seen as a proportioned version of the other blade.

Suppose one of the blades has a pitch error, theoretically this would feature different changes in the pressure profile as one might expect the profile to have a distinct shape to those seen in this study leading to a fault detection technique which is capable of identifying the type of fault present.

The results presented prove the capability of pressures recorded in the field of the rotor in identifying an asymmetric rotor. Furthermore, the signal processing performed indicates that it may aid future investigations to make comparisons in the averaged time and frequency domains. Time-domain results present pressure profiles which may be examined for specific faults based on the deviations observed. But with the information provided this cannot be confirmed.

4.2.3 Pressure Field Sensitivity

All of the pressure probe analyses which have been considered up until this point have been based on probes 0 to 5 in order to relate them to the experimental investigations. These probes were all located within close proximity of the blade plane and positioned in radial locations which represented the outer half of the rotor blades. The results discussed in this section compare amplitudes of the pressure profiles and their frequency components for probes located in other parts of the domain.

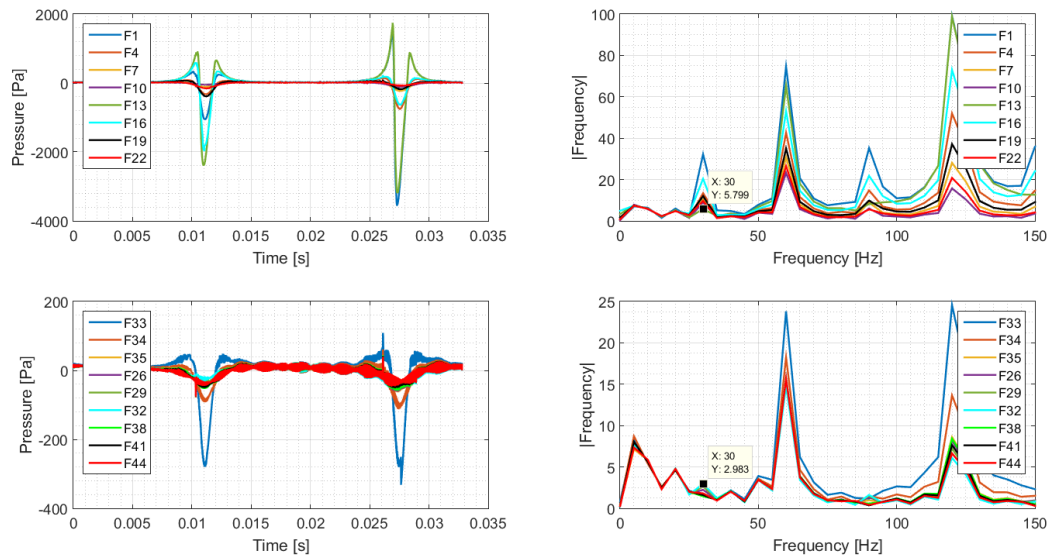


Fig. 16. Comparisons of faulty pressure profiles and frequencies at different probe locations.

From previous sections pressure probes 0 to 2 portrayed higher peak values in comparison to probes 3 to 5 which intuitively makes sense. Also, various results illustrated the inefficiency of the probes situated at the rotor tip in representing the pressure amplitudes found by the probes within the blade radius. This implies that probes at 67% and 80% of the radius predicted the anomaly better. Referring to Fig. 10 for the probe locations, pressures probed at 80% of the blade radius will be compared to assess the degradation in the fault detection as one moves perpendicularly away from the rotor blade (probes 10, 7, 4, 1, 13, 16, 19 and 22). Also, probes situated in the plane of the rotor but extended past its radius (probes 33, 34 and 35) shall be compared as well as pressures at locations far away from the blade radius and out of the rotor plane (32, 29, 26, 38, 41 and 44). Figure 16 shows the results of the pressures at each of these locations and its respective frequency transformations for the faulty rotor only.

Comparing the pressure profiles of the probes recorded in line at 80% of the faulty rotor radius expresses the decay in the troughs as the probes move perpendicularly away from the rotor blade. The trough representing the perfect blade of the faulty rotor deteriorates with minimum values of 3500, 752, 230 and 110 Pa for probes 1, 4, 7 and 10 respectively. This shows that at a perpendicular distance of 0.3 m away from the rotor blade, a pressure probe would need to detect a pressure fluctuation smaller than 110 Pa which could very well be lost to external interactions and noise in practical applications. Nevertheless, the numerical results show that even with the smaller peak values, the frequencies at these pressure probes demonstrate that they are still capable of establishing the existence of the asymmetry since there are peaks at the rotational frequency of the blade.

Probe 13 produces peculiar results as it is located in a region where it records pressures below the perfect tracking blade and above the mistracked blade as they pass. This explains its poor performance in detecting

the fault in the frequency domain having the smallest amplitude for these probes at a value of 5.8 for the rotational frequency. This probe is unrealistically situated and would not be used in any practical application.

Probes 16, 19 and 22 show similar trends to the probes discussed. However, these probes reflect the faulty blade as the higher of the two troughs for a single rotation. This is as a result of the probes being situated in the negative y-axis with the faulty blade passing nearer than the perfect blade. They show the same detection capabilities as the probes in the positive y-axis indicating frequency amplitudes at the 1/rev frequency.

Comparison of the results for all of the probes which extend further than the radius of the rotor signify inadequate fault detection. Not much can be distinguished in the pressure profiles plotted per rotation which is verified in the frequencies they produce. These probes do not identify the rotational frequency of the rotor well enough.

The results presented in this section recognised the incapability of detecting the fault using pressure probes located outside the radius of the rotor. It is seen that pressure measurements within the radius detect the fault appropriately. The loss in pressure peak values as measurements are acquired further away from the plane of the rotor are described. This concluded that the fault could be detected as one moved further away from the blade perpendicularly but results measured in practice would most likely be susceptible to other interactions and noise, skewing the results. One should also understand that the conclusions derived in this analysis are for the specialised case of a zero-pitched rotor and considering pressure information alone. A pitched rotor is bound to disturb the flow more and it is possible that other fluid dynamic quantities and noise can be acquisitioned in other locations depending on the phenomena and behaviours presented.

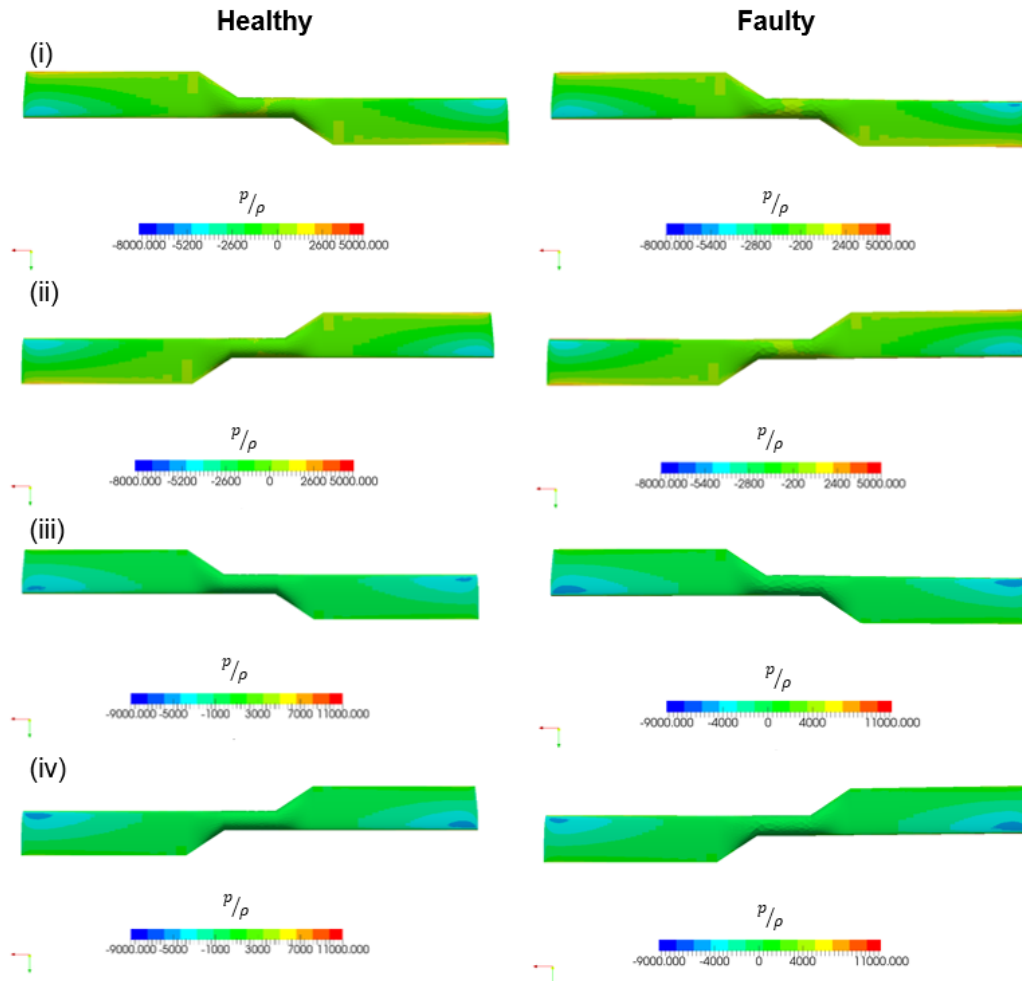


Fig. 17. Comparison of healthy and faulty pressures over the surface of the blade.

4.2.4 Blade Surface Pressure Comparisons

Figure 17 compares the surface pressures along the blade for the healthy and faulty rotor systems. All of the contours are taken from the last time instance of the respective simulations. Comparisons (i) and (iii) show the results in the same configuration but plotted on different scales, the faulty blade on the faulty rotor is the right-hand side blade with the fault imposed into the page. Comparisons (ii) and (iv) are given for the same configuration and represent the other side of the blade for configurations (i) and (iii) respectively. The fault in these instances are again on the right-hand side but protrude out of the page. The pressures are compared on different scales to show the fidelity for each pressure range used in observing the fault.

In all of the healthy instances, good symmetry is observed in the surface pressures between each of the blades. On the contrary, each of the faulty rotors show some irregularities between the blades. Figure 17 (i) shows a larger drop in pressure near the leading edge at the tip of the faulty blade for the specific pressure range. Although a vast difference can be seen between the healthy and faulty surface pressures for (iii), it is difficult to identify the fault by only comparing the blades of the faulty rotor as done for

(i). Similar comments can be given for the detection capabilities of (ii) and (iv) noting that (iv) performs better than (ii) which illustrates the effect that the specified pressure range has on observing the fault. The surface pressures also portray the difference in the pressure exhibited by the perfectly tracking blade of the faulty rotor (consider the left blade of comparison (iv)) from those on the healthy rotors which was explained in Section 4.2.2 as a result of the blades experiencing different upstream flows.

Implementation of a monitoring technique which uses pressure-sensitive paint to identify the presence of particular flow phenomena could be considered if it is feasible to observe the fault from the blade surface pressures. However, this would need to be considered carefully since the results established are particularly sensitive and in a practical environment may be incompetent due to noise and external interactions. Using pressure-sensitive paint may become costly depending on the size of the rotor considered and the wear resistance of the paint. Other considerations in the use of such a monitoring method would be the response time of the paint to pressure fluctuations as well as the manner in which the data would be acquired as it would most likely require a high-speed camera.

Still, this section expresses the plausibility of observing a fault by monitoring the surface pressures. The implications of using such a technique would have to be considered in further investigations understanding the fidelity of such a measurement technique. These conclusions are for the particular fault of mistracking where other geometric faults may demonstrate larger deviations, such as an incorrectly pitched blade.

5. CONCLUSION

Fault detection for a mistracking blade was assessed through an analysis of the rotor forces and moments, pressure signals probed in the field and from the pressure along the surface of the blades. The forces, moments and pressure signals detected the fault as increases in the 1/rev frequency amplitudes. The field recorded pressure signals could also be compared in the time-domain where the fault is identified as a deviation between the pressure profiles for the particular blade. The field pressure signals were compared for their efficacy based on where they were located. This concluded that recordings in the field of the rotor should be taken at radial locations representing the outer half of the blade but not past its tip and normal locations up to 0.3 m could detect the fault but will most likely be affected by other factors in practical applications. Comparison of the surface pressure contours concluded that blade asymmetry could be detected using this approach but a high level of fidelity is required in order to visualise and capture the specific fault.

This investigations primary objective was to assess what could be inferred about a fault from the flow field in order to determine the feasibility of fluid dynamic based fault detection for rotor systems. This study proves the ability of detecting rotor faults from fluid dynamic data but further investigation is required in order to determine whether a specific fault can be diagnosed. Detection of the rotor fault as increases in the 1/rev frequency components agrees with the literature on structural detection features but the introduction of fluid dynamic detection features means that aerodynamic based faults could be isolated and identified independently which is beneficial in the detection of rotor imbalance as well as the development of RTB algorithms and procedures.

The reader is provided with the following recommendations for future work:

- Although an economical model was developed with respect to the modelling decisions made, the simulations were still computationally intensive. Improvements could be made to the domain locations, the meshing strategy and resolution as well as the discretisation schemes to produce a model which is more stable and converges quicker.
- Geometric simplifications, such as the trim tabs, should be included to gauge their effect on the fault features.
- Other fault mechanisms should be studied in

order to identify whether they can be independently identified when monitoring.

- The sidebands detected in the experimental frequency domain were described as representing high-frequency flow phenomena or blade flap and could not be represented by the model. These phenomena need to be investigated further along with the effect it may have on the fault detection features.
- The effect that external interactions have on the results and consequently the fault detection features needs to be investigated.
- Experimental equipment and sampling frequency need to be selected carefully when using the techniques described in this study in order to ensure that the time-domain pressure profiles are resolved well.

ACKNOWLEDGEMENTS

I would like to thank the Centre for Asset Integrity Management (C-AIM) Group, the Centre for High-Performance Computing (CHPC), Denel Aerodynamics and Capital Equipment Group (CEG) for their support, guidance and resources over the duration of this work.

REFERENCES

- Allmark, M. (2016). *Condition monitoring and fault diagnosis of tidal stream turbines subjected to rotor imbalance faults*, PhD Thesis, Cardiff University, Cardiff, United Kingdom.
- Amenabar, I., A. Mendikute, A. López-Arraiza, M. Lizaranzu and J. Aurrekoetxea (2011). Comparison and analysis of non-destructive testing techniques suitable for delamination inspection in wind turbine blades. *Composites Part B: Engineering. Elsevier Ltd* 42(5), 1298–1305.
- Bechhoefer, E., A. Fang and E. Garcia (2014). Rotor Track and Balance Improvements. *Annual Conference of the Prognostics and Health Management Society*, 1–9.
- Bramwell, A. R. S., G. Done and D. Balmford (2000). *Bramwell's Helicopter Dynamics. Bramwell's Helicopter Dynamics*, 1–397.
- Conlisk, A. T. (1997). Modern helicopter aerodynamics. *Annual Review of Fluid Mechanics* 29(1), 515–567.
- Forbes, G. L. and R. B. Randall (2013). Estimation of turbine blade natural frequencies from casing pressure and vibration measurements. *Mechanical Systems and Signal Processing. Elsevier* 36(2), 549–561.
- García Márquez, F. P., A. M. Tobias, J. M. Pinar Pérez and M. Papaalias (2012). Condition monitoring of wind turbines: Techniques and methods. *Renewable Energy. Elsevier Ltd* 46, 169–178.

- Gwashavanhu, B., A. J. Oberholster and P. S. Heyns (2016). Rotating blade vibration analysis using photogrammetry and tracking laser Doppler vibrometry. *Mechanical Systems and Signal Processing*. Elsevier 76–77, 174–186.
- Hameed, Z., Y. S. Hong, Y. M. Cho, S. H. Ahn and C. K. Song (2009). Condition monitoring and fault detection of wind turbines and related algorithms: A review. *Renewable and Sustainable Energy Reviews* 13(1), 1–39.
- Kusnick, J., D. E. Adams and D. T. Griffith (2015). Wind turbine rotor imbalance detection using nacelle and blade measurements. *Wind Energy* 18(2), 267–276.
- Li, C., Q. Lin, X. Ding and X. Ye (2016). Performance, aeroacoustics and feature extraction of an axial flow fan with abnormal blade angle. *Energy*. Elsevier Ltd 103, 322–339.
- Lundstrom, T., J. Baqersad and C. Niezrecki (2016). Monitoring the Dynamics of a Helicopter Main Rotor With High-Speed Stereophotogrammetry. *Experimental Techniques* 40(3), 907–919.
- Oggiano, L., K. Boorsma, G. Schepers and M. Kloosterman (2016). Comparison of simulations on the NewMexico rotor operating in pitch fault conditions. *Journal of Physics: Conference Series*, 753(2).
- Ozbek, M., D. J. Rixen, O. Erne and G. Sanow (2010). Feasibility of monitoring large wind turbines using photogrammetry. *Energy*. Elsevier Ltd 35(12), 4802–4811.
- Pandey, K. M., G. Kumar, D. Das, D. Deka, A. Surana and H. J. Das (2012). CFD Analysis of an Isolated Main Helicopter Rotor for a Hovering Flight. *Volume 1: Advances in Aerospace Technology*. ASME, 543.
- Park, K. S., T. Asim and R. Mishra (2012). Computational fluid dynamics based fault simulations of a vertical axis wind turbines. *Journal of Physics: Conference Series*, 364(1).
- Pawar, P. M. and R. Ganguli (2007). Helicopter rotor health monitoring - A review. *Proceedings of the Institution of Mechanical Engineers, Part G: Journal of Aerospace Engineering* 221(5), 631–647.
- Renzi, M. J. (2004). *An Assessment of Modern Methods for Rotor Track and Balance*, MSc Thesis, Air Force Institute of Technology, Ohio, USA.
- Rumsey, C. (2016). NASA Langley Research Center: Turbulence Modeling Resource. [Online] Available at: https://turbmodels.larc.nasa.gov/naca0012_val.html [Accessed 25 September 2017].
- Singh, H. K., P. M. Pawar, R. Ganguli and S. Nam Jung (2008). On the effect of mass and stiffness unbalance on helicopter tail rotor system behavior. *Aircraft Engineering and Aerospace Technology* 80(2), 129–138.
- Strawn, R. C. and R. Biswas (1996). Numerical simulations of helicopter aerodynamics and acoustics. *Journal of Computational and Applied Mathematics* 66(1–2), 471–483.
- Stupar, S., A. Simonović and M. Jovanović (2012). Measurement and Analysis of Vibrations on the Helicopter Structure in Order to Detect Defects of Operating Elements. *Scientific Technical Review*, 62(1), 58–63.
- Xu, C. and R. S. Amano (2002). Unsteady Pressure Field Investigation of an Axial Fan—Blade Unsteady Pressure Field Measurement. *International Journal of Rotating Machinery* 8(6), 385–395.
- Xu, C., R. S. Amano and R. Perez (2002). Unsteady Pressure Field Investigation of an Axial Fan—Inlet and Outlet Unsteady Pressure Field Measurement. *International Journal of Rotating Machinery* 8(6), 375–383.
- Yang, B. and D. Sun (2013). Testing, inspecting and monitoring technologies for wind turbine blades: A survey. *Renewable and Sustainable Energy Reviews* 22, 515–526.